PHYSICAL REVIEW E **86**, 041904 (2012)

Structure of a micropipette-aspirated vesicle determined from the bending-energy model

Jeff Z. Y. Chen[*]

Department of Physics and Astronomy, University of Waterloo, Waterloo, Ontario, Canada, N2L 3G1

(Received 16 May 2012; revised manuscript received 11 September 2012; published 8 October 2012)

The structure of the system consisting of an aspirating pipette and an aspirated vesicle is investigated with fixed total vesicle volume, total vesicle surface area, and aspirated volume fraction, based on the bending-energy model. Through an energetic consideration, the usage of an aspirated volume fraction can be converted to the aspirating pressure for the determination of a phase diagram; the procedure identifies a first-order transition, between a weakly aspirated state and the strongly aspirated state, as the pressure increases. The physical properties of the system are obtained from minimization of the bending energy by an implementation of the simulated annealing Monte Carlo procedure, which searches for a minimum in a multivariable space. An analysis of the hysteresis effects indicates that the experimentally observed aspirating and releasing critical pressures are related to the location of the spinodal points.

DOI: 10.1103/PhysRevE.86.041904 PACS number(s): 87.16.D−, 87.80.Fe, 46.70.Hg

I. INTRODUCTION

In a typical pipette (micropipette) experiment, a suction pressure Δp is applied through a circular opening of radius a that touches a particular portion of a vesicle. The vesicle can be partially pulled into the tube, driving up its overall bending energy because of the shape distortion (see Fig. 1). For years, the method has been used to experimentally probe and characterize the mechanical properties of cells, lipid-membrane vesicles, and even double emulsion-templated polymersomes (see, e.g., Refs. [2–13]). In addition, pipette aspiration is a popular method used to hold a vesicle in place in applications of other recent experimental techniques such as optical trapping [14–16]. Typically, a vesicle-aspiration experiment produces a suction-pressure versus projection-length curve. Some theoretical interpretations of the experimental results are available [2,17,18].

An interesting case is the discontinuous transition between a weakly aspirated state [Figs. 1(d)–1(f)] and a strongly aspirated state [Figs. 1(g)–1(i)] as the suction pressure rises. The work in this paper identifies this as a first-order transition, based on the solution of the Helfrich bending-energy model [19,20], which has been used for studying the conformation properties of a free vesicle [1,21], vesicle adhesion to external particles and environments [22–32], and vesicle conformation distortion under an external strain [33–37]. The numerical solution indicates that the spinodal stability limits associated with the first-order transition correspond to the stability pressure limits observed experimentally, previously referred to as the critical suction and leasing pressures. Some of the concepts introduced in this work are similar to those demonstrated in Ref. [38], where the authors considered a simple toy model for the vesicle, neglecting the bending rigidity.

Instead of the suction pressure, the present work uses the volume fraction between the volume of the vesicle portion inside the pipette and the total vesicle volume as the basic parameter in the calculation. The suction pressure, which is a conjugate thermodynamic property, is then derived from the derivative of the bending energy with respect to the volume fraction. The procedure allows for the identification of the phase transition in terms of a physical quantity similar to the Gibbs free energy in liquid-gas theory, which can be used to guide the discussion of the weak to strong aspiration transition. The approach taken here can be contrasted with a recent work on the same subject by Das [18], who directly used the suction pressure. In addition, the approach avoids his ansatz of single-point contact between the shape curve and the interior pipette wall to treat the strong aspiration regime [see Fig. 1(b) in Ref. [18]]. As shown below, the conformation determined in this work is substantially different from this ansatz.

In addition, the present work also demonstrates the usefulness of a computational technique in minimizing a multivariable vesicle energy with multiple constraints—in total internal volume, surface area, aspirated volume fraction, and a constraint that deals with the hard-wall excluding condition. The numerical challenge is attacked by a simulated annealing Monte Carlo procedure, which locates the approximate energy minimum in a controlled precision. No further approximations and assumptions are made in this work.

The paper is organized such that all technical materials are presented in Appendixes. The basic formalism for an axisymmetric vesicle theory is reviewed in Sec. II. The numerical treatment, including the simulated annealing Monte Carlo approach [39], is briefly described in Secs. II B and II C and discussed more thoroughly in Appendixes A, B, and C. An example of the weak to strong aspirating transition of a prolate shape is discussed in Sec. III C and then compared with experimental observations in Sec. III D. Two more examples, the weak oblate to strong prolate transition and the weak stomatocyte to strong prolate transition, are discussed in Sec. III E. A more complete three-dimensional phase diagram, shown in two dimensions with one parameter fixed, is discussed in Secs. III F and III G. The throughput region (discussed in Sec. III A) and the full aspiration limit (discussed in Sec. III H) of the phase diagram can be approximately dealt

---

[*] jeffchen@uwaterloo.ca

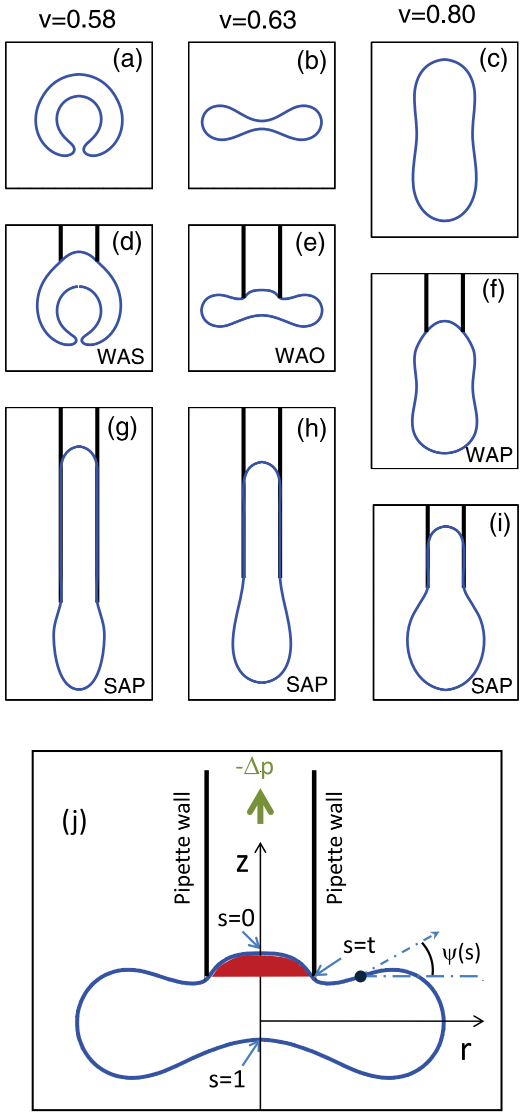

FIG. 1. (Color online) Conformation of a vesicle in a free state for (a) $v = 0.58$, (b) $v = 0.63$, and (c) $v = 0.80$; in a weakly aspirated state for (d) $v = 0.58$, (e) $v = 0.63$, and (f) $v = 0.80$; and in a strongly aspirated state for (g) $v = 0.58$, (h) $v = 0.63$, and (i) $v = 0.80$. The definition of the reduced volume v is given in Eq. (6) and is the only relevant physical parameter for the structure of a free vesicle [1]. The coordinate system used in this work is illustrated in (j). The volume trapped inside the pipette, corresponding to the shaded (red) potion, is $V_{\text{in}} = uV$, where V is the vesicle's total volume. A pressure difference Δp is assumed between the pressures outside and inside the pipette. In (d)–(i) the reduced pipette radius $a/r_0 = 3/8$ is used, where $r_0 = \sqrt{A/4\pi}$ with A the total vesicle surface area. The numerical calculation was performed with fixed A, V, and u.

with by analytical estimations, as presented in Appendixes D and E.

II. MODEL

In this section the energy model is described in detail and the numerical approach is discussed briefly. Numerical techniques are further explained in Appendixes A–C.

A. Bending energy

For a fluid-membrane vesicle having no spontaneous curvature, the Helfrich bending-energy model is used,

$$E_b = 2\kappa \oint M^2 dA, \tag{1}$$

where M is the mean of the two local principle curvatures of the membrane, κ is the bending modulus, and the integral over the area element dA covers the entire closed surface. In general, for a biomembrane κ is large compared to the thermal energy at room temperature; hence the vesicle is assumed to adopt a conformation corresponding to the global minimum of E_b for a fixed enclosing volume V and surface area A [19,20].

This paper focuses on the axisymmetric system only. In terms of the coordinate system in Fig. 1(j), a vesicle shape can be described by the angle $\psi(s)$, where s is an arc variable measured from the top of the vesicle where $s = 0$ to the bottom where $s = 1$, and $\psi(s)$ is the angle between the tangent direction of the shape curve and the r axis. Then the bending energy can be written as

$$E_b = \kappa\pi \int_0^1 (\dot{\psi} + \sin\psi/r)^2 r\, ds, \tag{2}$$

under the constraint

$$\dot{r} = \cos\psi(s), \tag{3}$$

where a dotted symbol represents the derivative with respect to s. In terms of this coordinate system, the enclosed volume and surface area of the vesicle can be expressed by

$$A = S^2 \int_0^1 ds\, 2\pi r \tag{4}$$

and

$$V = S^3 \int_0^1 ds\, \pi r^2 \sin\psi. \tag{5}$$

Note that both s and r are dimensionless in this formalism. The length scale of the problem is accounted for by the total contour length S, which appears in these two constraints. From a scaling analysis, one can show that E_b/κ is a function of a single parameter, the reduced volume

$$v = 6\sqrt{\pi} V/A^{3/2}, \tag{6}$$

for a free vesicle problem [1].

B. Numerical schemes for a free vesicle

The minimization of E_b under constraints (3)–(5) can be tackled by various numerical approaches. One can, for example, convert the functional-minimization problem into a formalism similar to Hamiltonian dynamics in classical mechanics, with the incorporation of the constraints by Lagrangian multipliers. In particular, a surface-tension-like multiplier Σ and a pressurelike Lagrangian multiplier Π were used for constraints in Eqs. (4) and (5) and the minimization was then carried out in the Π-Σ ensemble. The calculation of the bending energy as a function of A and V was then transformed back into an A-V ensemble [1]. In another approach, the unknown function $\psi(s)$ was modeled by its Fourier transformation with undetermined

Fourier coefficients. The bending energy and the constraints were all written as functions of these coefficients and the direct minimization of Eq. (2) could be performed to pin down these coefficients [40]. In a recent paper, the usage of a target energy that includes E_b as the first term and incorporates all three constraints (3)–(5) by direct energy penalties was introduced [37]; the coefficients of the penalty terms can be used to control the precision of the calculation.

From numerical solutions emerge three different branches of the free energy of a free vesicle, corresponding to stomatocyte [Fig. 1(a)], oblate [Fig. 1(b)], and prolate [Fig. 1(c)]; the stomatocyte is stable in the parameter regime $v = [0, v_{\rm SO}]$, oblate in $v = [v_{\rm SO}, v_{\rm OP}]$, and prolate in $v = [v_{\rm OP}, 1]$, where according to Ref. [1]

$$v_{\rm SO} = 0.5915, \tag{7}$$

$$v_{\rm OP} = 0.6516, \tag{8}$$

which is also confirmed in our recent work by using a similar numerical approach [32] and the target-energy approach [37].

C. Pipette-aspirated vesicle

The computation carried out in this work is based on the minimization of the target function

$$\tilde{E}_{\rm target} = E_b/\kappa + \Lambda_V \left(\frac{S^3}{V} \int_0^1 \pi r^2 \sin\psi \, ds - 1 \right)^2 + \Lambda_A \left(\frac{S^2}{A} \int_0^1 2\pi r \, ds - 1 \right)^2 + \Lambda_{\rm in} \left(\frac{S^3}{V_{\rm in}} \int_0^t \pi r^2 \sin\psi \, ds - 1 \right)^2, \tag{9}$$

where t is the value of s at which the shape curve makes contact with the aperture edge of the pipette. In this formalism, $\psi(s)$ is assumed yet to be determined and $r(s)$ is related to $\psi(s)$ by integrating over Eq. (3). The last integral in Eq. (9), together with the S^3 prefactor, represents the volume of the shaded (red) portion of the vesicle trapped inside the pipette opening $V_{\rm in} \equiv uV$, shown in Fig. 1(j). Once the target energy is minimized with large penalty coefficients Λ_V, Λ_A, and $\Lambda_{\rm in}$, the terms in the large parentheseseffectively yield constraints on the total enclosed volume V, surface area A, and trapping volume $V_{\rm in}$, which need to be considered in the current system.

Another important constraint that needs to be invoked in the current problem is the fact that

$$Sr(s) \leqslant a \tag{10}$$

for all $s \leqslant t$. This constraint describes the hard-wall condition for the vesicle portion trapped inside the pipette, which can be rather simply implemented together with the selection of the variable t in the simulated Monte Carlo protocol, explained in Appendix C.

Although the search of the target-energy minimum is Monte Carlo based, in an ideal situation when the final simulated temperature goes to zero and the total Monte Carlo steps approach infinity, one expects the convergence to the exact location of a minimum. The validity of the numerical method may be checked by forcing $\Lambda_{\rm in} = 0$, which reproduces the original free-vesicle problem. The current calculation, using the procedure described in Appendixes A and B, gives

$$v_{\rm SO} = 0.595 \pm 0.003, \tag{11}$$

$$v_{\rm OP} = 0.638 \pm 0.003, \tag{12}$$

which are comparable to the benchmark values in Eqs. (7) and (8). The difference can be attributed to the finite number of nodes ($N + 1 = 201$) and final simulated inverse temperature ($\beta = 1 \times 10^4$) taken in the numerical procedure as described in the Appendixes; the difference, however, does not affect the physical picture presented below. In this paper, the simulated Monte Carlo procedure, together with the usage of a simulated β, is a technique used to determine the minimum of the target energy; it does not reflect the thermal fluctuations seen in this system at a finite temperature.

III. RESULTS AND DISCUSSION

The results presented in this section are based on a numerical solution of the bending energy model presented in Sec. II C, modified from Eq. (2) to take into account the physical picture of pipette aspiration. The discussion also incorporates some analytical results from the Appendixes as well.

A. Throughput region

The first division of the parameter space is between the aspiration region and throughput region. The latter corresponds to relatively large a/r_0 where any weak suction pressure can pull the entire vesicle through the pipette opening. Within the current model, the threshold for the reduced pipette radius $a_{\rm th}/r_0$, beyond which the vesicle can be entirely sucked through the pipette, is a function of reduced volume v only. The length scale r_0 is related to the surface area A of the vesicle and is defined as

$$r_0 = \sqrt{A/4\pi}. \tag{13}$$

An analysis of the throughput vesicle under the assumption that it is made of a cylindrical part and two capping half spheres (Appendix E) reveals that the dividing curve can be analytically approximated by

$$v = (3/2)(a_{\rm th}/r_0) - (1/2)(a_{\rm th}/r_0)^3, \tag{14}$$

where $a_{\rm th}$ is implicity expressed in v. Graphically, this is shown by the solid (red) curve in Fig. 2. Overlapping on the curve are the symbols representing the direct numerical solution to Eq. (9) that divides the $V_{\rm in} = V$ (throughput) and $V_{\rm in} < V$ (aspiration) regions. The agreement between the curve and data validates the assumption made in predicting Eq. (14).

B. Energy in the aspiration region

Within the current approach, the minimized reduced bending energy E_b/κ depends on three parameters: the reduced volume v in Eq. (6), the reduced aperture radius a/r_0, and the trapped volume fraction

$$u = V_{\rm in}/V, \tag{15}$$

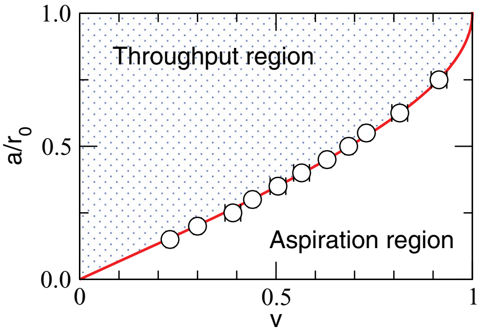

FIG. 2. (Color online) The solid (red) curve is an analytic *estimate* [Eq. (E2)] that divides the system into a throughput region where the entire vesicle is pulled through the pipette even under a weak aspirating pressure and an aspiration region where the vesicle is aspirated at the pipette tip, as shown in Fig. 1. Circles are the *exact* numerical solution to the problem.

where $V_{\rm in}$ is the volume of the vesicle trapped *inside* the pipette [the shaded (red) part in Fig. 1(j)]. This v-a/r_0-u ensemble is more convenient for discussion and can be converted to the v-a/r_0-$\tilde{P}$ ensemble used in the experimental setting, where

$$\tilde{P} \equiv V\Delta p/8\pi\kappa, \tag{16}$$

with Δp being the difference between pressures outside and inside the pipette.

The analysis carried out below is based on an interpretation of the numerical solution for the reduced bending energy

$$\tilde{E}_b \equiv E_b/8\pi\kappa = \tilde{E}_b(v,a/r_0,u) \tag{17}$$

as a function of u. Up to three branches of $\tilde{E}_b$ are typically seen in the numerical solution, depending on the magnitude of v and a/r_0.

Moving to the v-a/r_0-$\tilde{P}$ ensemble, we can deduce the $\tilde{P}$ required to maintain a trapped volume fraction u, utilizing the virtual work principle,

$$\tilde{P} = \partial\tilde{E}_b/\partial u. \tag{18}$$

The stability of a conformation is now analyzed through comparing the minimum of the Legendre transformation of $\tilde{E}_b$, similar to the notion in thermodynamics,

$$\tilde{G} \equiv \tilde{E}_b - \tilde{P}u, \tag{19}$$

which takes into account the work performed to pull a vesicle volume of $V_{\rm in}$ into the pipette under an aspiration pressure $\tilde{P}$.

C. Aspirating a prolate shape

As the first example, the $\tilde{E}_b$ and $\tilde{P}$ curves are shown in Figs. 3(a) and 3(b) for $v = 0.80$ and $a/r_0 = 3/8$. Originally, at $\tilde{P} = 0$, the vesicle shows a prolate shape [see Fig. 1(c)], corresponding to the energy minimum in Fig. 3(a). Because of the convex vesicle shape at the top, shown in Fig. 1(c), there is already a nonzero u.

We discuss the physical properties in terms of an increasing u. As the trapped volume fraction u starts to increase, the conformation makes a weak distortion from the perfect prolate, maintaining a weakly aspirated prolate (WAP) shape as shown in Fig. 1(f). The bending energy rises correspondingly from the minimum. After the vesicle forms a tubular portion inside the pipette, the bending energy cost for pulling the vesicle further into the pipette, by increasing u, rises only slowly. Near the final stage, in the strongly aspirated prolate (SAP) regime, the tubular portion becomes significant, as illustrated in Fig. 1(i). At the final stage, the bending energy increases drastically, diverging at the aspiration limit u^*, a limit that will be further discussed in Sec. III H.

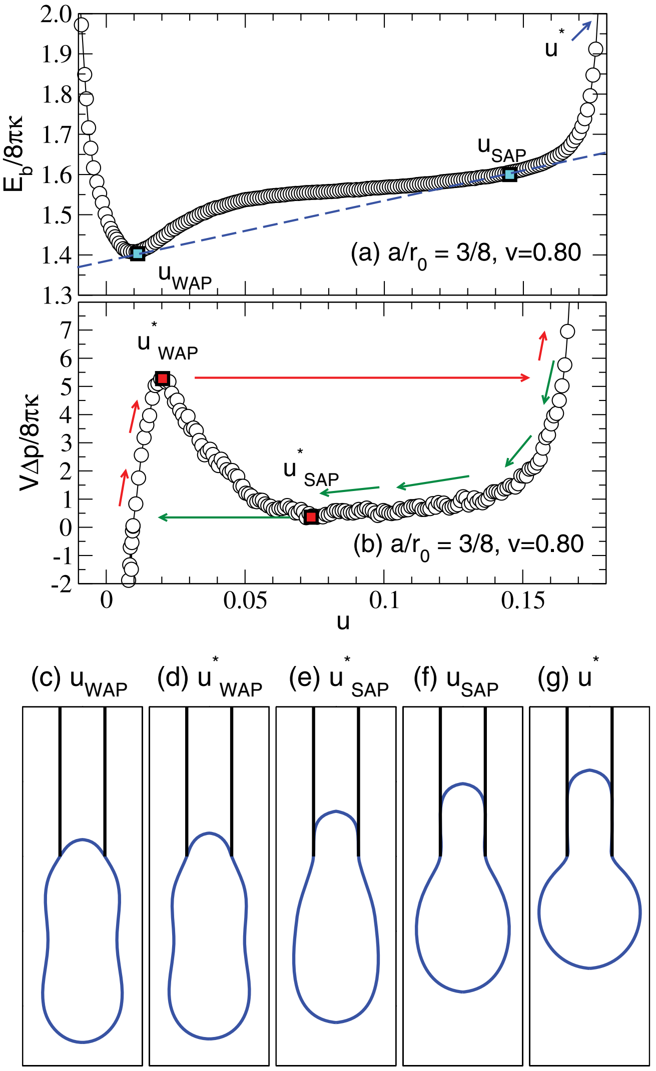

FIG. 3. (Color online) (a) Solution of the bending energy E_b as a function of the trapped volume fraction u in Eq. (15) for $a/r_0 = 3/8$ and $v = 0.80$. Circles correspond to distorted conformations originated from a prolate vesicle. (b) Reduced aspiration pressure (16) as a function of u, which was calculated from Eq. (18). Configurations at specific values of u, to be discussed in Secs. III C and III D, are plotted in (c)–(g).

Can we determine the stable structure, now using $\tilde{P}$ instead of u as the varying parameter? An interesting application of the bending-energy curve is the determination of the first-order phase transition between WAP [Fig. 1(f)] and SAP [Fig. 1(i)] as $\tilde{P}$ increases. A relatively small aspiration pressure keeps the system in a WAP state. With increasing $\tilde{P}$, the vesicle shape further distorts until a transition pressure is reached, after which the system displays a SAP state, characterized by a jump in u at the transition point. The trapped volume fractions $u_{\rm WAP}$ and $u_{\rm SAP}$ where the transition occurs are determined from the conditions

$$\tilde{P}(u_{\rm WAP}) = \tilde{P}(u_{\rm SAP}), \tag{20}$$

$$\tilde{G}(u_{\rm WAP}) = \tilde{G}(u_{\rm SAP}). \tag{21}$$

Because $\tilde{P}$ is the slope of the $\tilde{E}_b$ curve, a simple technique for determining $u_{\rm WAP}$ and $u_{\rm SAP}$ can be developed on an energy plot such as Fig. 3(a); a double-tangent line can be constructed in lieu of solving Eqs. (20) and (21), as illustrated by the long-dashed line in the figure; the two tangent points are $u_{\rm WAP}$ and $u_{\rm SAP}$. The slope itself is the reduced WAP-SAP transition pressure $\tilde{P}_{\rm WAP\text{-}SAP}$. In the phase-transition theory, $u_{\rm WAP}$ and $u_{\rm SAP}$ are referred to as the binodal points for a first-order phase transition.

D. Experimental hysteresis in a WAP-SAP transition

An inspiring comparison can be made between Fig. 3(b) and the PV diagram of the van der Waals gas; both pressure curves show the existence of a maximum and a minimum. These spinodal points, defined in the plot as $u^*_{\rm WAP}$ and $u^*_{\rm SAP}$, indicate the stability limits in a real experimental setting where $\tilde{P}$ is the control parameter.

A typical aspirating experiment can be described by following the up (red) arrows in Fig. 3(b). As the suction pressure $\tilde{P}$ increases from 0, the system may pass the WAP-SAP transition point, as illustrated in Fig. 3(c) for $u_{\rm WAP}$, running into a metastable region. Before or when the system hits the stability limit, as illustrated in Fig. 3(d) for $u^*_{\rm WAP}$, a jump in u to a value beyond $u_{\rm SAP}$ takes place (i.e., a sudden increase of the aspiration length in the pipette) following the long arrow line in the plot. The configuration looks similar to Fig. 3(f), but with a somewhat longer aspiration length. The jump accompanies a $\tilde{P}^*_{\rm WAP}$ that is larger than $\tilde{P}_{\rm WAP\text{-}SAP}$; a further increase of $\tilde{P}$ after the jump yields only a small increase of u.

A typical releasing experiment can be described as well, but now following the down (green) arrows in Fig. 3(b). As $\tilde{P}$ decreases from a large value, the system may pass the SAP-WAP transition point, illustrated in Fig. 3(f) for $u_{\rm SAP}$. Within the range $[u^*_{\rm SAP}, u_{\rm SAP}]$ the system is in a metastable state, where a decreasing $\tilde{P}$ reduces the aspiration length (or u) in the tube, as shown by the (green) arrows. Before or when the system hits the stability limit [illustrated in Fig. 3(e) for $u^*_{\rm SAP}$] a jump of u to a small value takes place, following the long (green) arrow in the plot. The jump now accompanies a $\tilde{P}^*_{\rm SAP}$ that is smaller than $\tilde{P}_{\rm WAP\text{-}SAP}$ and may immediately release the entire vesicle from the pipette aperture after the jump.

Characteristics of these hysteresis effects have been detected in experiments with comparable behavior in $\tilde{P}^*$ and the projection length, which can be identified with u through

$$L \approx V_{\rm in}/\pi a^2 = uV/\pi a^2. \tag{22}$$

In experimental papers [2,10], the pressure at the jumping point ($\tilde{P}^*_{\rm WAP}$ or $\tilde{P}^*_{\rm SAP}$ for either aspirating or releasing) is always referred to as the critical pressure. The usage of the word "critical" has a specific meaning in the phase-transition theory. Now, from the current analysis, by realizing that we are looking at the hysteresis effects of a first-order phase transition, these usages of "critical pressure" should not be confused with the specific meaning associated with a continuous phase transition. These pressures actually correspond to the spinodal pressures.

In a recent theoretical study of the same bending energy model for an axisymmetric vesicle, Das solved the shape equation, i.e., the force equilibrium equation or Euler's equation for $\psi(s)$ by minimizing E_b. He introduced an additional assumption that allows the shape curve inside the tube to touch the wall by a single point [18]. This can be contrasted with the current approach where no such assumption was introduced. As matter of fact, the numerical solution of the SAP phase in the current work shows that the shape curve displays a significant segment in contact with the interior wall [see examples in Figs. 1(g)–1(i)]. Because of the additional assumptions taken by Das, two separate pressure curves were produced; this can be contrasted with the single continuous curve in Fig. 3(b). Table I shows some further differences between the current and his results. Furthermore, he suggested that the critical aspiration pressure corresponds to a maximum in the aspiration pressure-projection length curve and the critical releasing pressure corresponds to a minimum in the curve; this notion coincides with the spinodal picture explained above.

To summarize, there are a number of characteristic pressures discussed above. This paper identifies the micropipette aspiration as a first-order phase transition from a weakly aspirated state to a strongly aspirated state, at a transition pressure $\tilde{P}_{\rm WAP\text{-}SAP}$. This pressure may not be directly observed in experiments because of hysteresis effects. Instead, two characteristic spinodal pressures are observable: $\tilde{P}^*_{\rm WAP}$ ($>\tilde{P}_{\rm WAP\text{-}SAP}$) and $\tilde{P}^*_{\rm SAP}$ ($<\tilde{P}_{\rm WAP-SAP}$); the former is an instability edge in a suction experiment (the critical aspiration pressure) and the latter is an instability edge in a releasing experiment (the critical releasing pressure). For different a/r_0 these characteristic pressures are shown in Fig. 4(a).

TABLE I. Comparison of the reduced spinodal pressures $\tilde{P}^*_{\rm WAP}$ and $\tilde{P}^*_{\rm SAP}$ and the reduced spinodal projection lengths $\tilde{\ell}^*_{\rm WAP}$ and $\tilde{\ell}^*_{\rm SAP}$ from the current work with those of Ref. [18]. Here $\tilde{\ell} = \ell/r_0$, where the projection length ℓ was read directly from the numerical shape function. The numbers in the third and seventh columns were converted from the original table by a factor of $v/3$ by taking into account the different reduced units used.

v	$\tilde{P}^*_{\rm WAP}$	$\tilde{P}^*_{\rm WAP}$ [18]	$\tilde{\ell}^*_{\rm WAP}$	$\tilde{\ell}^*_{\rm WAP}$ [18]	$\tilde{P}^*_{\rm SAP}$	$\tilde{P}^*_{\rm SAP}$ [18]	$\tilde{\ell}^*_{\rm SAP}$	$\tilde{\ell}^*_{\rm SAP}$ [18]
0.75	495 ± 10	641.4	0.099 ± 0.005	0.057	101 ± 10	70.8	0.25 ± 0.01	0.39
0.85	846 ± 10	727.2	0.100 ± 0.005	0.057	112 ± 10	80.8	0.25 ± 0.01	0.39
0.95	1116 ± 20	838.2	0.100 ± 0.005	0.057	117 ± 10	89.4	0.25 ± 0.01	0.39

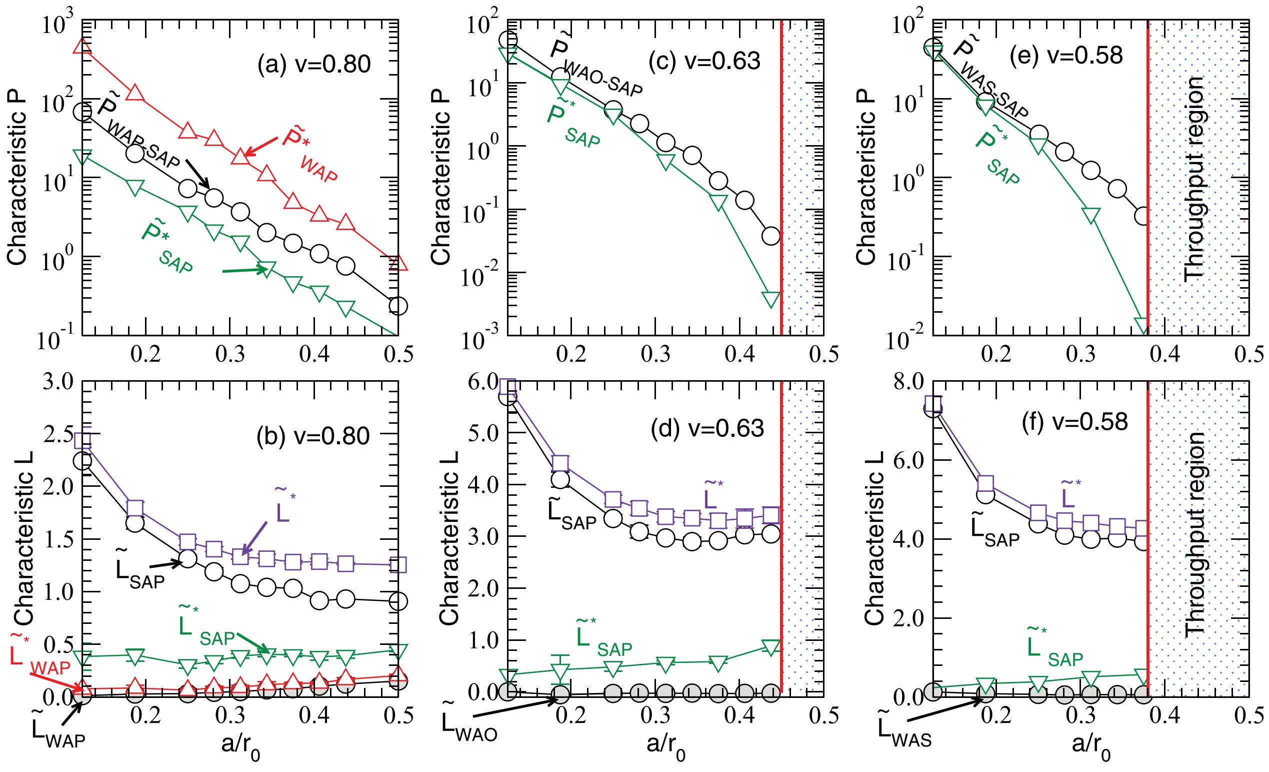

FIG. 4. (Color online) Characteristic pressures and projection lengths predicted from the bending energy model for $v = 0.80$ [(a) and (b)], 0.63 [(c) and (d)], and 0.58 [(e) and (f)]. The first-order transition pressure is represented by the line associated with circles in (a), (c), and (e); the binodal boundaries for the projection length are presented by the lines associated with open and shaded (gray) circles in (b), (d), and (f); the suction and releasing stability limits are described by $\tilde{P}$, represented by the lines associated with the up and down triangles in these plots, respectively; the corresponding spinodal lines are presented in (b), (d), and (f) by the up and down triangles as well. The full aspiration limit is indicated by squares in (b), (d), and (f).

E. Aspirating an oblate or stomatocyte shape

Another example of the energy curve is shown in Fig. 5 for $a/r_0 = 3/8$ and $v = 0.63$, where the original free vesicle adopts the oblate [Fig. 1(b)] conformations. The undistorted state corresponds to the energy minimum of the oblate branch in Fig. 5(a). The prolate branch, shown in the plot by the curve associated with circles, still exists. A noticeable feature is the competition between the energy minima; at $\tilde{P} = 0$, the lowest determines the stable free-vesicle conformation, hence the prolate conformation is only metastable.

At a weak $\tilde{P}$, the system displays the weakly aspirated oblate (WAO) conformation, shown in Fig. 1(e). As $\tilde{P}$ increases, a first-order WAO-SAP phase transition takes place, where the SAP state at the transition is shown in Fig. 1(h). The procedure used in Sec. III C for the determination of the transition point can be used here as well by requiring

$$\tilde{P}(u_{\mathrm{WAO}}) = \tilde{P}(u_{\mathrm{SAP}}), \tag{23}$$

$$\tilde{G}(u_{\mathrm{WAO}}) = \tilde{G}(u_{\mathrm{SAP}}), \tag{24}$$

where the functions on the left-hand sides are taken from the oblate branch and those on the right-hand sides are from the prolate branch. Graphically, a double-tangent construction, shown in Fig. 5(a) by the long-dashed line, can be used directly on the figure for the determination of u_{WAO}, u_{SAP}, and $\tilde{P}_{\mathrm{WAO\text{-}SAP}}$.

The experimentally observed hysteresis effects can be partially accounted for by the pressure curves in Fig. 5(b) as well. Upon the initial weak suction, an oblate shape can pass through the binodal u_{WAO} transition point [illustrated in Fig. 5(c)], staying in the oblate branch, as indicated by the up (red) vertical arrow. However, the WAO branch of the pressure curve, which is now separated from the SAP branch [see Fig. 5(b)], monotonically increases and does not display a maximum in contrast to the first half of the curve in Fig. 3(b). In other words, a spinodal $\tilde{P}^*_{\mathrm{WAO}}$ cannot be directly identified; how a WAO jumps to SAP at or before the stability limit u^*_{WAO} is unclear in the current work. In comparison with the discussion in Sec. III D, we can only guess qualitatively that a similar procedure can take place where the system arrives at a SAP shape following the long arrow in the figure. A question mark has been placed in Fig. 5(b) for the exact location of the critical aspiration pressure and its corresponding configuration in Fig. 5(d).

The releasing experiment following the down (green) arrows, however, can be quantitatively described; the vesicle may stay in the prolate branch within $[u^*_{\mathrm{SAP}}, u_{\mathrm{SAP}}]$, displaying a configuration intermediate to Figs. 5(e) and 5(f), until it reaches the stability limit as illustrated in Fig. 5(e) for u^*_{SAP}. Once the pressure is further lowered, the aspirated vesicle may disembark the pipette and convert itself back to an oblate shape. These hysteresis effects have been previously observed in experiments as well (see, e.g., Ref. [2]).

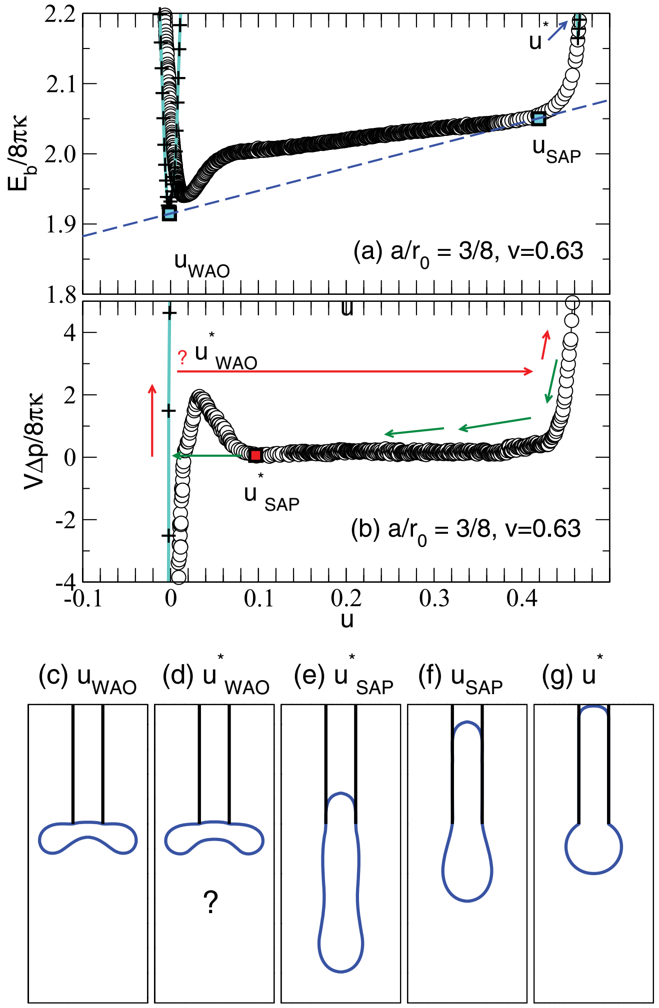

FIG. 5. (Color online) Solution of the bending energy E_b as a function of the reduced trapped volume u for (a) $a/r_0 = 3/8$ and $v = 0.63$. Circles and plus signs correspond to distorted conformations originated from prolate and oblate vesicles, respectively. (b) Reduced aspiration pressure (16) as a function of u, which was calculated from Eq. (18). Configurations at several u are illustrated in (c)–(g) and discussed in Sec. III E.

The above discussion analyzed the WAO-SAP phase transition. Starting from a free stomatocyte, a similar analysis can be conducted for the transition between a weakly aspirated stomatocyte (WAS) and a SAP in reference to Fig. 6, but it is not repeated here.

F. Phase diagram

In Secs. III C–III E the structural properties for a fixed $a/r_0 = 3/8$ and three typical values of v were discussed. The complete phase diagram, however, is three dimensional, depending on $v, a/r_0$, and $\tilde{P}$. In this section we first examine the a/r_0-$\tilde{P}$ phase diagram for three values of v and then the v-$\tilde{P}$ phase diagram for three values of a/r_0.

The circles in Fig. 4(a) defines the first-order phase boundary for the case of $v = 0.80$: Above the boundary, the SAP state is stable and below the boundary the WAP state is stable. The corresponding transition points, now described by a reduced projection length

$$\tilde{L} = u/(a/r_0)^2, \tag{25}$$

are shown in Fig. 4(b) by shaded circles at the WAP state and by open circles at the SAP state. Here $\tilde{L}$ is proportional to the experimentally measurable projection length l in a strongly aspirated state; in a weakly aspirated state, the definition of the projection length l itself is not precise.

The spinodal suction pressure $\tilde{P}^*_{\rm WAP}$ discussed above (the critical suction experiment) is shown by the up triangles, which is generally greater than $\tilde{P}_{\rm WAP\text{-}SAP}$. The releasing stability limit $\tilde{P}^*_{\rm SAP}$ is shown by the down triangles, which is generally lower

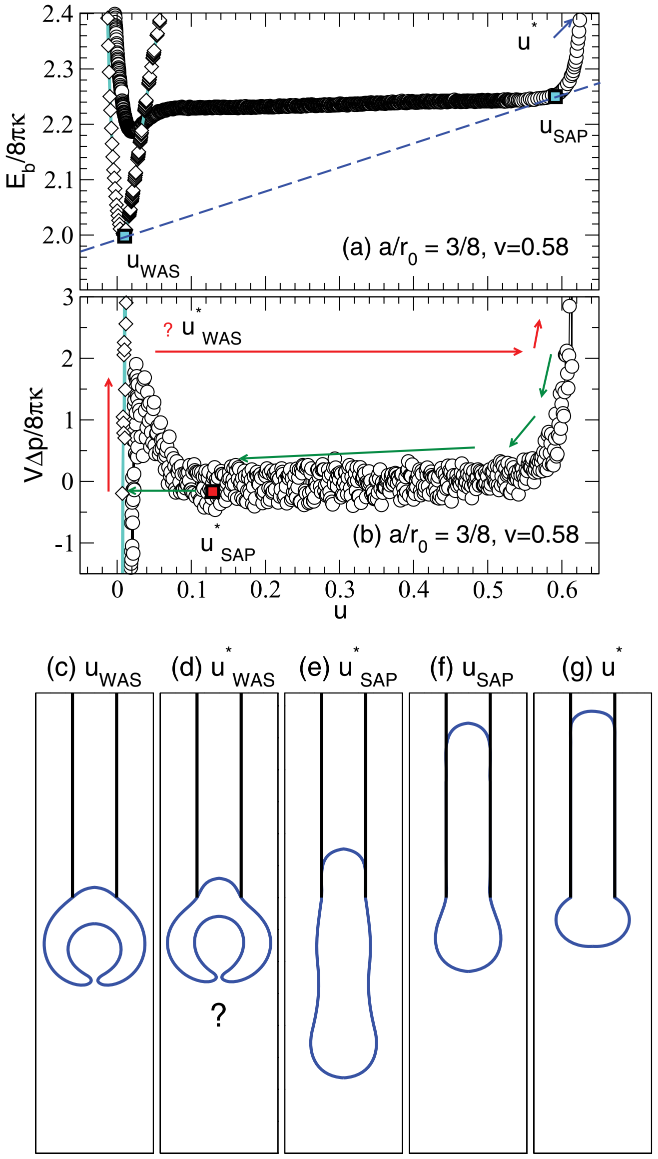

FIG. 6. (Color online) Solution of the bending energy E_b as a function of the reduced trapped volume u for (a) $a/r_0 = 3/8$ and $v = 0.58$. Circles and diamonds correspond to distorted conformations originated from prolate and stomatocyte vesicles, respectively. (b) Reduced aspiration pressure (16) as a function of u, which was calculated from Eq. (18). Configurations at several u are illustrated in (c)–(g).

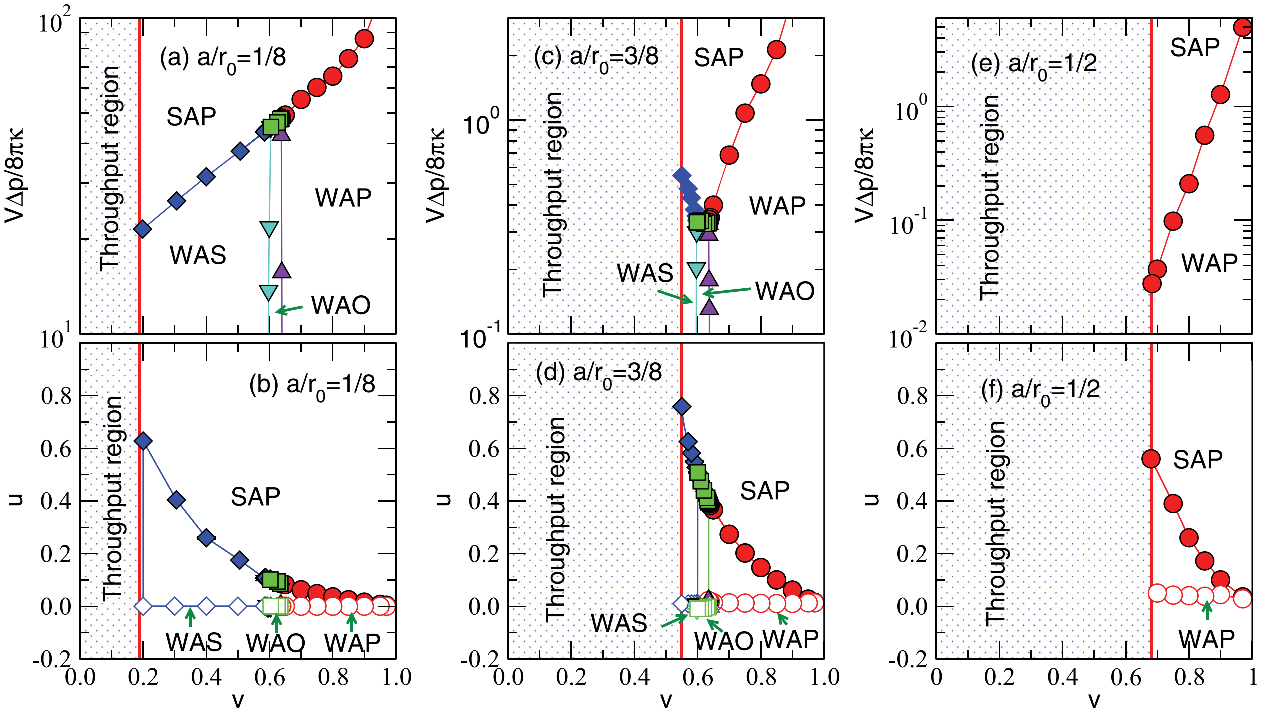

FIG. 7. (Color online) Three examples of the $\tilde{P}$-v [(a), (c), and (e)] and u-v [(b), (e), and (f)] phase diagrams for (a) and (b) $a/r_0 = 1/8$, (c) and (d) 3/8, and (e) and (f) 1/2. Illustrations of representative conformations of the SAP, WAP, WAO, and WAS states can be found in Fig. 1.

than the first-order transition pressure. Note the logarithmic scale used in the $\tilde{P}$ plot. In a suction experiment after the system reaches $\tilde{P}^*_{\mathrm{WAP}}$, $\tilde{L}$ [up triangles in Fig. 4(b)] jumps to a state with a value higher than the open circles; in a releasing experiment after the systems reaches $\tilde{P}^*_{\mathrm{SAP}}$, $\tilde{L}$ [down triangles in Fig. 4(b)] jumps to a state with a lower value than the shaded circle. In addition, the full suction limit u^*, beyond which the vesicle cannot be further pulled into the pipette, is represented by the squares in Fig. 4(b), in terms of the projection length.

The circles in Fig. 4(c) define the first-order phase boundary $\tilde{P}_{\mathrm{WAO\text{-}SAP}}$ for the case of $v = 0.63$: Above the boundary, the SAP state is stable and below the boundary the WAO state is stable; the binodal phase boundaries, in terms of the reduced projection length, are shown by the shaded and open circles in Fig. 4(d), corresponding to the WAO and SAP boundaries, respectively. Because the current calculation cannot quantitatively describe the spinodal point in a suction experiment for the WAO-SAP transition, $\tilde{P}^*_{\mathrm{WAO}}$ is not specified in the plot. However, we can determine the releasing stability boundary $\tilde{P}^*_{\mathrm{SAP}}$, assuming that the SAP conformation is maintained in the releasing experiment, by the method described in Sec. III E; the boundary is represented in Fig. 4(c) by the down triangles; the corresponding $\tilde{L}^*_{\mathrm{SAP}}$, below which the transition will take $\tilde{L}$ to a value lower than the shaded circles in Fig. 4(d), is also shown by down triangles. The squares in Fig. 4(d) represent the full suction limit u^*. In comparison with Figs. 4(a) and 4(c), now we see the emergence of the throughput region (dotted area) in the phase diagram for relatively large a/r_0.

The third example is presented in Figs. 4(e) and 4(f). Many features are similar to Figs. 4(c) and 4(d), but now for the transition between WAS and SAP. The discussion is omitted here.

We now turn to the discussion of the $\tilde{P}$-v phase diagrams for given $a/r_0 = 1/8$, 3/8, and 1/2, shown in Fig. 7. The numerical results for the WAP-SAP phase boundaries are displayed by circles in Figs. 7(a), 7(c), and 7(e). The corresponding phase boundaries u_{WAP} and u_{SAP} are plotted in Figs. 7(b), 7(d), and 7(f) by open and solid circles, respectively.

In the $v_{\mathrm{SO}} < v < v_{\mathrm{OP}}$ and $v < v_{\mathrm{SO}}$ regions, under a weakly aspirating pressure, the WAO state [Fig. 1(d)] and the WAS state [Fig. 1(e)] are stable, respectively. As $\tilde{P}$ increases, the system undergoes a first-order WAO-SAP transition and a first-order WAS-SAP transition to conformations illustrated in Figs. 1(g) and 1(h), respectively. The transition pressure for the WAO-SAP transition is displayed by squares in Figs. 7(a) and 7(c); the corresponding trapped volume fractions at the WAO-SAP transition (u_{WAO} and u_{SAP}) are displayed in Figs. 7(b) and 7(d) by open and solid squares. The transition pressure for the WAS-SAP transition is displayed by diamonds in Figs. 7(a) and 7(c) and the trapped volume fractions at the WAS-SAP transition (u_{WAS} and u_{SAP}) are displayed in Figs. 7(b) and 7(d) by open and solid diamonds. Overall, the aspiration region in each of the pressure phase diagrams may be divided into four regions: SAP, WAP, WAO, and WAS.

The phase diagram presented in Fig. 7 is preempted by the throughput condition numerically presented in Fig. 2 or Eq. (E2). The dotted regions of the plots in Fig. 7 correspond to the same throughput region described in Fig. 2, but from a different perspective; the location of the vertical boundary in v for the three values $a/r_0 = 1/8$, 3/8, and 1/2 can be readily identified from the phase boundary in Fig. 2. For clarity, only the phase boundaries are plotted in Fig. 7; the spinodal boundaries discussed above are not plotted explicitly in this figure.

G. Fine structure

The two dividing phase boundaries, between WAS and WAO (down triangles in Fig. 7) and between WAO and WAP (up triangles in Fig. 7), are not exactly vertical in the $\tilde{P}$-v phase diagram. In a narrow region just below v_{OP}, $v \lesssim v_{\mathrm{OP}}$, the system undergoes two transitions between three phases (WAO, WAP, and SAP), sequentially as $\tilde{P}$ increases. Similarly, in a narrow region just above v_{SO}, $v \gtrsim v_{\mathrm{SO}}$, the system undergoes two transitions between three phases (WAS, WAO, and SAP), sequentially as $\tilde{P}$ increases. These fine structures in the phase diagram would be difficult to detect experimentally because of the narrow ranges and hence are not described further in this paper.

H. Fully aspirated limit

One common feature of the WAP-SAP, WAO-SAP, and WAS-SAP transitions is that after transitions the system arrives at a strongly aspirated prolate shape, shown in Figs. 1(g)–1(i). If $\tilde{P}$ further rises, the vesicle continuously changes its shape until it reaches a fully aspirated limit. A typical conformation is shown in Fig. 8(b), where the vesicle portion outside the pipette starts to show a conformation resembling a perfect sphere.

Numerically, the bending-energy curve diverges as the strong aspiration limit is approached, as indicated in Figs. 3(a), 5(a), and 6(a) by arrows. The maximum trapped volume fraction u^* can be identified from these plots and depends on both v and a/r_0. The numerical results are summarized in Fig. 8, where $u^*(v,a/r_0)$ is plotted as a function of v for $a/r_0 = 1/2$, $3/8$, $1/4$, and $1/8$ by circles, squares, diamonds, and plus signs, respectively.

For small a/r_0, we may use the approximation that treats the trapped vesicle portion [i.e., the shaded (red) portion in Fig. 8(b)] as a cylinder and the outside portion as a perfect sphere. This allows us to estimate u^* as a function of v and a/r_0, as presented in Appendix D. The estimate, now expressed in an analytic form (D6), is shown by solid curves in Fig. 8(a) for various values of a/r_0. There is good agreement between Eq. (D6) and the numerical results, in particular for small a/r_0. Hence Eq. (D6) can be used as the estimate for the location of the fully aspiration limit.

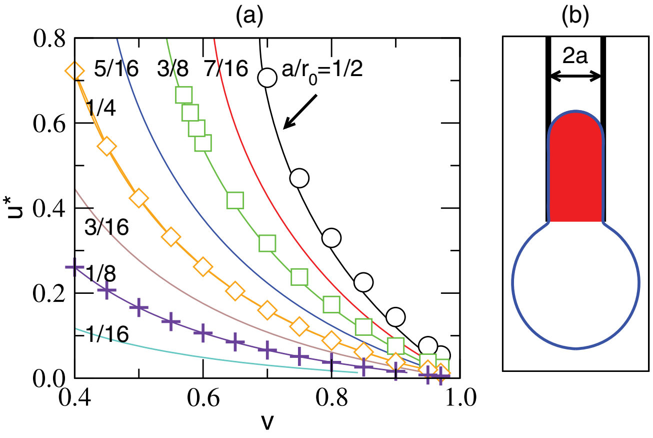

FIG. 8. (Color online) (a) Limit of full aspiration, in terms of the maximum trapped volume fraction u^* as a function of the reduced vesicle volume v, for various values of a/r_0 and (b) an example of the numerical solution for a strongly aspirated vesicle. The solid curves were produced from the analytical result (D6), based on a sphere-tube ansatz in Appendix D. The symbols were obtained from a direct numerical analysis of the bending-energy curves, such as those displayed in Figs. 3, 5, and 6.

IV. CONCLUSION

In summary, a simulated annealing Monte Carlo procedure that minimizes the bending energy of a vesicle with fixed internal volume, surface area, and trapped volume inside the pipette was employed to study the structure of a vesicle aspirated by a micropipette. The usage of the trapped volume fraction is shown to be an effective tool that determines the first-order transition gap between a weakly aspirated structure and the strongly aspirated prolate shape. We have shown that the so-called critical aspiration and releasing pressures, both observed experimentally, can be accounted for by the physical picture of spinodal stability, associated with a first-order phase transition. The prediction of the phase diagrams, presented in Figs. 4 and 7, in light of the concepts previously introduced in Refs. [18,38], can be tested by a carefully conducted experiment such as the one recently reported in Ref. [10]. It is hoped that such experiments will be able to reveal new physical features in a classical technique of manipulating vesicles.

A number of other physical effects can influence the structures and phases predicted in this work. Bozic *et al.* [41] and Heinrich *et al.* [42] studied the effects due to the finite bilayer thickness for more realistic features of a vesicle under an external strain. In addition to E_b, a thickness-related term was included. Another possible effect is the short-range attraction between the vesicle surface and the pipette interior wall, produced from a hydrophobic interaction when the vesicle makes contact with the wall. These effects are neglected here for simplicity, but can be included in a further extension of the present work.

ACKNOWLEDGMENTS

The author thanks Natural Sciences and Engineering Research Council for providing financial support and SHARCNET for providing computational time. The author also thanks Sovan Das for a delightful discussion about the differences and similarities in the approaches taken between Refs. [18,28] and the current work.

APPENDIX A: DISCRETIZATION

The model presented in Secs. II B and II C is based on a continuous description of the shape curve, specified by the function $\psi(s)$ (where $s = [0,1]$) and a scaling parameter S. For numerical computation, we divide the continuous variable s into N equally spaced parts with an increment $\Delta s = 1/N$.

The spatial position of these nodes is represented by the coordinates (r_i, z_i), where $i = 1,2,3,\ldots,N+1$ and $r_1 = r_{N+1} = 0$. These nodes connect N pieces of linearly connected straight segments of equal length Δs. The shape function $\psi(s)$ is approximated by the series of variables ψ_i, where $i = 1,2,3,\ldots,N$. Based on an starting position (r_1, z_1), coordinates

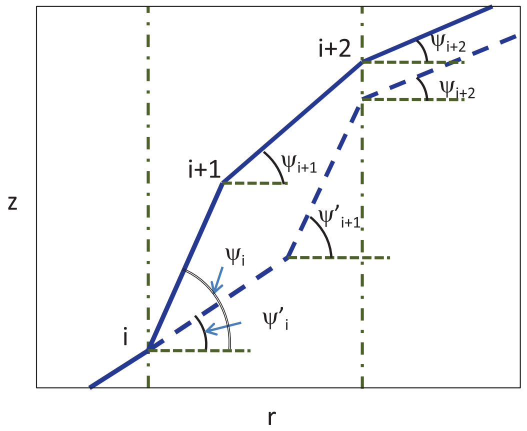

FIG. 9. (Color online) Discretization of the shape curve into N segments and $N+1$ nodes as illustrated by the solid lines. The long-dashed lines represent a typical Monte Carlo move where both angles ψ_i and ψ_{i+1} are changed to ψ_i' and ψ_{i+1}' in order to keep r_{i+2} and ψ_{i+2} unchanged in the move.

of all nodes can be written

$$r_{i+1} = r_i + \Delta s \cos \psi_i \tag{A1}$$

and

$$z_{i+1} = z_i + \Delta s \sin \psi_i , \tag{A2}$$

where $i = 1,2,3,\ldots,N$. The solid lines in Fig. 9 illustrate a discretized curve.

The bending energy is then approximated by a summation

$$\frac{E_b}{\kappa} = \pi \Delta s \sum_{i=2}^{N} \left\{ \frac{\psi_i - \psi_{i-1}}{\Delta s} + \frac{\sin[(\psi_{i-1} + \psi_i)/2]}{r_i} \right\}^2 \times r_i + f_1 + f_{N+1}. \tag{A3}$$

The last two terms f_1 and f_{N+1} capture the bending-energy contributions from the top and bottom parts of the closed surface, respectively. The shape of the top part is assumed to be a spherical cap of height $|z_1 - z_2|$, whereas the center of this hypothetical sphere is located along the z axis and the spherical surface intersects the first two nodes (r_1,z_1) and (r_2,z_2). The bending energy f_1 required was produced from this cap representation. The same assumption, but now for the last two points, was made to produce f_{N+1}. Other integrals in Eq. (9) were treated in a similar way.

APPENDIX B: SIMULATED ANNEALING

The basic idea of the simulated annealing approach is to use a target energy in a Monte Carlo simulation by moving variables (i.e., $\{\psi_i\}$) from an initial guess to the location of the minimum in a stochastic process generally heading towards a downhill direction on average. A temperature is used to regulate the thermal fluctuations and finally decreases to a low value to effectively freeze the system energy into the global minimum [39].

In this work, at a Monte Carlo update, a node i was randomly selected and an attempt to move the variable ψ_i was made by adding or subtracting a small random angle; the coordinates of the $(i+1)$th node (r_{i+1},z_{i+1}) are then updated; the adjacent angle ψ_{i+1} was also adjusted accordingly to guarantee that r_{i+2} of the $(i+2)$th node is unchanged. This requirement is crucial to ensure that after the propagation of calculating r_j $(j = i+1, i+2, \ldots, N+1)$ from Eq. (A1), we must eventually keep $r_{N+1} = 0$. The value of the target energy E_{target}' was then determined from the attempted configuration; a Boltzmann weight $\exp[-\beta(E_{\text{target}}' - E_{\text{target}})]$ was in turn used as the transition probability in a standard Metroplis Monte Carlo algorithm [43] for the acceptance of the newly generated configuration. Every configuration-change attempt was intercalated by an attempt for scale change: S was moved by a random small number. Such a scale change has no effect on the bending energy, but was proven necessary to minimize the penalty terms in the target-energy function.

To simulate an annealing process, the Boltzmann factor β was arranged to increase from 20 to a final value of 1×10^4, in a typical production run that contained $10^6 N$ attempted updates. An initial guess of $\{\psi_i\}$ was selected so that the ending node is exactly sitting on the z axis, $r_{N+1} = 0$. Results in this paper were produced by using $N = 200$.

APPENDIX C: SEARCHING FOR *t*

For a given set of coordinates (r_i,z_i), where $i = 1,2,3,\ldots,N+1$, we started with $i = 1$, which always has $r_1 = 0$. Sequentially going through the nodes starting from $i = 1$, we then searched for the first node (the kth node), which has a radius greater than the pipette radius a, $r_k > a$. A linear interpolation between the coordinates r_{k-1}, z_{k-1}, and r_k,z_k was then assumed and the position on the line that satisfies $r = a$ determined the contact point t together with the z coordinate of the pipette opening Z_p. The entire set (r_i,z_i) was redefined by shifting the reference value of the z coordinate, $z_i \Leftarrow z_i - Z_p$.

The last integral in Eq. (9), which together with the S^3 prefactor represents the trapped vesicle volume, can then be approximated by a summation based on the rectangular rule, starting from the second node to the $(k-1)$th node. Additionally, the contribution to the integral from the first node to the second node was treated by assuming a spherical cap described in Appendix A; the contribution to the integral from the $(k-1)$th node to the $s = t$ point was approximated by a trapezoidal rule.

The algorithm adjusts the contact position t as the representative nodes move in a Monte Carlo simulation. In the undesirable case where a Monte Carlo attempt generates a configuration containing an intersecting node k much different from a stable intersecting point, the large penalty term in Eq. (9) rules out the new configuration during the important sampling process. This implies that small Monte Carlo moves are desirable, which was controlled by the size of the random angle selected for a Monte Carlo attempt. This size (usually small) was adjusted such that the acceptance rate of a Monte Carlo segment fell between 40% and 60%.

The constraint in Eq. (10) is automatically satisfied by this algorithm. No additional steps are needed in the simulation.

APPENDIX D: STRONG ASPIRATION LIMIT

Consider a pipette with a small radius a in comparison with the characteristic length scale of the vesicle r_0. In the strong aspiration limit, we assume that (i) the part of the vesicle that is trapped inside the pipette can be approximated by a cylinder of radius a and length L and (ii) the part of the vesicle that is outside the pipette can be approximated by a perfect sphere. The following estimate yields the trapped volume fraction u^* in terms of v and a/r_0.

From assumption (i), the surface area A' and volume V' of the trapped portion can be written as

$$A' = 2\pi a L \tag{D1}$$

and

$$V' = \pi a^2 L, \tag{D2}$$

where we have kept the leading terms only. We then have $A' = 2V'/a$. Hence the ratio

$$\frac{A'}{A} = \frac{2V'}{a}\frac{A^{1/2}}{A^{3/2}} = \frac{2V'}{a}\frac{r_0\sqrt{4\pi}}{6\sqrt{\pi}V/v} = \frac{2vu^*}{3}\frac{r_0}{a}. \tag{D3}$$

From assumption (ii), the effective reduced volume is 1 for a perfect sphere,

$$6\sqrt{\pi}(V - V')/(A - A')^{3/2} = 1, \tag{D4}$$

which gives

$$v(1 - u^*)/(1 - A'/A)^{3/2} = 1. \tag{D5}$$

Inserting Eq. (D3) into Eq. (D5) yields an implicit equation for the function $u^*(v,a/r_0)$,

$$v(1 - u^*) = [1 - (2r_0/3a)vu^*]^{3/2}, \tag{D6}$$

which is valid in the $a/r_0 \ll 1$ region. For various values of the ratio a/r_0, u^* is plotted as a function of v by solid curves in Fig. 8.

APPENDIX E: THROUGHPUT LIMIT

Consider a system in the strong aspiration limit where the ratio between the trapped volume and the total vesicle volume is u^*, as described in Appendix D. In general, u^* goes up as a/r_0 increases, until u^* reaches 1 when $a = a_{\rm th}$. Any larger a allows the entire vesicle to move inside the pipette. Hence the throughput limit can be deduced from Eq. (D6) by setting $u^* = 1$, which yields

$$v = \frac{3}{2}\frac{a_{\rm th}}{r_0}, \tag{E1}$$

which is valid for systems having $a_{\rm th}/r_0 \ll 1$ because of the first assumption used in Appendix D.

Now a more careful treatment of the full $a_{\rm th}/r_0$ range can be made by assuming that the shape of a fully aspirated vesicle inside the pipette is made of a cylinder and two ending hemispherical caps. This consideration yields an implicit expression for $a_{\rm th}/r_0$ as a function of v,

$$v = \frac{3}{2}\frac{a_{\rm th}}{r_0} - \frac{1}{2}\left(\frac{a_{\rm th}}{r_0}\right)^3. \tag{E2}$$

The expression is valid for the entire range of $a_{\rm th}/r_0$ and is plotted as a solid curve in Fig. 2.

---

[1] U. Seifert, K. Berndl, and R. Lipowsky, Phys. Rev. A **44**, 1182 (1991).
[2] R. P. Rand and A. C. Burton, Biophys. J. **4**, 115 (1964).
[3] R. Waugh and E. A. Evans, Biophys. J. **26**, 115 (1979).
[4] A. Yeung and E. Evans, Biophys. J. **56**, 139 (1989).
[5] D. V. Zhelev, D. Needham, and R. M. Hochmuth, Biophys. J. **67**, 696 (1994).
[6] D. V. Zhelev, D. Needham, and R. M. Hochmuth, Biophys. J. **67**, 720 (1994).
[7] G. M. Artmann, K. L. Sung, T. Horn, D. Whittemore, G. Norwich, and S. Chien, Biophys. J. **72**, 1434 (1997).
[8] N. Fa, C. M. Marques, E. Mendes, and A. P. Schroder, Phys. Rev. Lett. **92**, 108103 (2004).
[9] C. T. Lim, E. H. Zhou, A. Li, S. R. K. Vedula, and H. X. Fu, Mater. Sci. Eng. C **26**, 1278 (2006).
[10] A. Tian, C. Johnson, W. Wang, and T. Baumgart, Phys. Rev. Lett. **98**, 208102 (2007).
[11] K. A. Rodowicz, H. Francisco, and B. Layton, Chem. Phys. Lipids **163**, 787 (2010).
[12] E. H. Zhou, S. T. Quek, and C. T. Lim, Biomech. Model Mechanobiol **9**, 563 (2010).
[13] N. P. Kamat, M. H. Lee, D. Lee, and D. A. Hammer, Soft Matter **7**, 9863 (2011).
[14] Y. Chen, B. Liu, G. Xu, and J.-Y. Shao, Cell. Mol. Bioeng. **2**, 351 (2009).
[15] B. Sorre, A. Callan-Jones, J.-B. Manneville, P. Nassoy, J.-F. Joanny, J. Prost, B. Goud, and P. Bassereau, Proc. Natl. Acad. Sci. USA **106**, 5622 (2009).
[16] M. Heinrich, A. Tian, C. Esposito, and T. Baumgart, Proc. Natl. Acad. Sci. USA **107**, 7208 (2010).
[17] E. Evans and W. Rawicz, Phys. Rev. Lett. **64**, 2094 (1990).
[18] S. Das, Phys. Rev. E **82**, 021908 (2010).
[19] U. Seifert, Adv. Phys. **46**, 13 (1997).
[20] M. Müller, K. Katsov, and M. Schick, Phys. Rep. **434**, 113 (2006).
[21] H. J. Deuling and W. Helfrich, J. Phys. (Paris) **37**, 1335 (1976).
[22] U. Seifert and R. Lipowsky, Phys. Rev. A **42**, 4768 (1990).
[23] T. R. Weikl, Eur. Phys. J. E **12**, 265 (2003).
[24] M. Deserno, Phys. Rev. E **69**, 031903 (2004).
[25] M. Deserno, J. Phys.: Condens. Matter. **16**, S2061 (2004).
[26] M. M. Muller, M. Deserno, and J. Guven, Europhys. Lett. **69**, 482 (2005).
[27] M. M. Muller, M. Deserno, and J. Guven, Phys. Rev. E **76**, 011921 (2007).
[28] S. Das and Q. Du, Phys. Rev. E **77**, 011907 (2008).
[29] S. Mkrtchyan, C. Ing, and J. Z. Y. Chen, Phys. Rev. E **81**, 011904 (2010).
[30] J. Z. Y. Chen and S. Mkrtchyan, Phys. Rev. E **81**, 041906 (2010).
[31] J. Z. Y. Chen, Y. Liu, and H. J. Liang, Phys. Rev. Lett. **102**, 168103 (2009).

[32] S. Cao, G. Wei, and J. Z. Y. Chen, Phys. Rev. E **84**, 050901(R) (2011).

[33] D. K. Fygenson, J. F. Marko, and A. Libchaber, Phys. Rev. Lett. **79**, 4497 (1997).

[34] T. R. Powers, G. Huber, and R. E. Goldstein, Phys. Rev. E **65**, 041901 (2002).

[35] I. Derenyi, F. Julicher, and J. Prost, Phys. Rev. Lett. **88**, 238101 (2002).

[36] A.-S. Smith, E. Sackmann, and U. Seifert, Phys. Rev. Lett. **92**, 208101 (2004).

[37] J. Z. Y. Chen, Phys. Rev. E **85**, 061910 (2012).

[38] S. Das, A. Tian, and T. Baumgart, J. Phys. Chem. B **112**, 11625 (2008).

[39] S. Kirkpatrick, C. D. Gelatt, and M. P. Vecchi, Science **220**, 671 (1983).

[40] W. T. Gozdz, Langmuir **23**, 5665 (2007).

[41] B. Bozic, S. Svetina, and B. Zeks, Phys. Rev. E **55**, 5834 (1997).

[42] V. Heinrich, B. Bozic, S. Svetina, and B. Zeks, Biophys. J. **76**, 2056 (1999).

[43] N. Metropolis, A. W. Rosenbluth, M. N. Rosenbluth, A. H. Teller, and E. Teller, J. Chem. Phys. **21**, 1087 (1953).